CellPress

Developmental Cell
Article

A Predictive Model of Bifunctional Transcription Factor Signaling during Embryonic Tissue Patterning

Jan Philipp Junker,[1,2] Kevin A. Peterson,[3] Yuichi Nishi,[3] Junhao Mao,[4] Andrew P. McMahon,[3] and Alexander van Oudenaarden[1,2,*]

[1]Departments of Physics and Biology, Massachusetts Institute of Technology, Cambridge, MA 02139, USA
[2]Hubrecht Institute, KNAW, and University Medical Center Utrecht, 3584 CT Utrecht, the Netherlands
[3]Department of Stem Cell Biology and Regenerative Medicine, Eli and Edythe Broad Center for Regenerative Medicine and Stem Cell Research, University of Southern California Keck School of Medicine, Los Angeles, CA 90089, USA
[4]Department of Cancer Biology, University of Massachusetts Medical School, Worcester, MA 01605, USA
*Correspondence: a.vanoudenaarden@hubrecht.eu
http://dx.doi.org/10.1016/j.devcel.2014.10.017

SUMMARY

Hedgehog signaling controls pattern formation in many vertebrate tissues. The downstream effectors of the pathway are the bifunctional Gli transcription factors, which, depending on hedgehog concentration, act as either transcriptional activators or repressors. Quantitatively understanding the interplay between Gli activator and repressor forms for patterning complex tissues is an open challenge. Here, we describe a reductionist mathematical model for how Gli activators and repressors are integrated in space and time to regulate transcriptional outputs of hedgehog signaling, using the pathway readouts *Gli1* and *Ptch1* as a model system. Spatially resolved measurements of absolute transcript numbers for these genes allow us to infer spatiotemporal variations of Gli activator and repressor levels. We validate our model by successfully predicting expression changes of *Gli1* and *Ptch1* in mutants at different developmental stages and in different tissues. Our results provide a starting point for understanding gene regulation by bifunctional transcription factors during mammalian development.

INTRODUCTION

During embryonic development, cell fate decisions must be tightly controlled in space and time. Gene expression in development often combines inputs from multiple upstream regulators in order to ensure proper formation of complex tissues and organs (Buecker and Wysocka, 2012; Levine, 2010). To understand cellular responses to upstream signaling factors, it is important to know the relation between regulator concentrations and target gene expression, termed the gene's input function. In single-cell organisms or cultured cells, the combined effect of different regulators has been determined experimentally by measuring the expression level for a gene of interest under varying concentrations of its different regulators (Kaplan et al., 2008; Kim and O'Shea, 2008; Setty et al., 2003). In multicellular organisms, however, it is often impossible to manipulate regulator levels with the necessary precision, precluding direct experimental measurement of input functions in the tissue context. Despite these limitations, input functions have been determined in intact *Drosophila melanogaster* embryos based on measurements of upstream regulators and downstream targets combined with thermodynamic models or machine learning algorithms (Segal et al., 2008; Zinzen et al., 2009). Knowledge of input functions allows predicting the expression of a given target gene based solely on analysis of upstream control factors. Yet, in many cases, the upstream regulators are essentially hidden variables, as their spatial distribution cannot be directly measured in intact tissues and organs. Thus, solving the inverse problem and determining the levels of upstream regulators based on expression patterns of downstream targets is an important challenge. Inferring hidden control variables will be essential for understanding design principles of gene regulation in the context of developmental pattern formation.

Cell-cell signaling pathways controlling the establishment of gene expression patterns in embryonic development are important examples of hidden control variables in gene expression. While these pathways differ significantly in their biochemical details, most of them share a striking common design principle: the majority of these pathways (e.g., Hedgehog, Wnt, Notch, and nuclear receptors) culminate in bifunctional transcription factors that act as either activators or repressors, with the balance between activating and repressing functions being controlled by signaling levels (see Figure S1A available online) (Barolo and Posakony, 2002). In many cases, it is not possible to determine levels of activating and repressing isoforms independently in intact tissues and with high spatial resolution. Modeling-based studies in *Drosophila melanogaster* suggest that activators and repressors may interact in complex ways to establish developmental gene expression patterns (Haskel-Ittah et al., 2012; Parker et al., 2011). Thus, determining the spatiotemporal variation of activating and repressing factors, and understanding how they are integrated to control target gene expression, will be critical for elucidating how precision and robustness are encoded during embryonic pattern formation.

The functional dualism of activator versus repressor control is established in its purest form in hedgehog signaling, where the

Gli proteins, a family of transcription factors that serve as the main downstream effectors of the hedgehog pathway, can act as either transcriptional activators or repressors. In the developing neural tube—one of the best studied model systems for hedgehog signaling in vertebrates (Dessaud et al., 2008)—Sonic hedgehog (Shh) is initially secreted from the notochord to establish a ventral-to-dorsal (VD) morphogen gradient. Shh controls the balance between Gli activator and Gli repressor via a cascade of negative interactions involving the transmembrane proteins Patched1 (Ptch1) as hedgehog receptor and Smoothened (Smo) as secondary signal transducer (Figure 1A). The Shh gradient regulates the patterned expression of cell fate determinants in the ventral half of the neural tube, leading to an intricate pattern of molecularly distinct neural progenitor stripes (Figure 1B). The importance of measuring spatiotemporal profiles of the Gli activator and repressor individually is becoming increasingly clear (Oosterveen et al., 2012), yet robust readouts that can discriminate between the activating versus repressing form of Gli proteins are currently unavailable. In addition, it remains unclear how activating and repressing forms of Gli are integrated for regulating individual target genes.

Mus musculus has three different Gli proteins, Gli1–3, which recognize very similar target sequences, but differ in their potencies as activators and repressors (Hui and Angers, 2011). Immunoblotting experiments with mouse embryo extracts have shown that Gli proteins are differentially processed upon hedgehog signaling (Pan et al., 2006). Specifically, Gli3 is the only mammalian Gli protein that can exert strong repressor function, whereas all three Gli proteins can act as transcriptional activators. This provides us with the unique possibility to manipulate activator and repressor levels with high precision by studying knockouts for individual Gli proteins.

Here, we present a minimal model for the dependence of the canonical hedgehog readouts *Gli1* and *Ptch1* on Gli activator and repressor levels. Based on highly quantitative and spatially resolved measurements of *Gli1* and *Ptch1* transcript levels, we solve the inverse problem and calculate the hidden control variables, Gli activator and repressor as a function of VD position (Figure 1C). We validate our reductionist approach by predicting expression changes of readout genes in mutants with modified activator and repressor levels. Furthermore, we use this technique to study the dynamics of activator and repressor levels, and we demonstrate that our model can also be applied to hedgehog signaling in the mouse forelimb.

RESULTS

Spatially Resolved Quantitative Gene Expression Analysis of Intact Mouse Neural Tube Sections

The hedgehog pathway components *Gli1* and *Ptch1* serve as readouts of pathway activity and are directly controlled by Gli binding sites (Vokes et al., 2007). These two genes are ideal candidates for studying activator and repressor control in hedgehog signaling: (1) their expression is not restricted to specific tissues; (2) there is no indication for major regulatory contributions by other signaling pathways; and (3) they are not part of the network of cross-repressive interactions that encompasses most of the cell fate determinants in the neural tube (Dessaud et al., 2008). In order to measure absolute transcript levels of *Gli1* and *Ptch1* in intact tissue, we designed single-molecule fluorescence in situ hybridization (smFISH) probes targeting these two genes. Probe sequences are provided in Table S1. Using an array of fluorescently labeled oligonucleotide probes complementary to the coding sequence of the genes, we were able to visualize and count individual mRNA molecules as diffraction-limited spots in cryosections of mouse embryos (Figures 1D, S1B, and S1C) (Itzkovitz et al., 2012; Raj et al., 2008). At embryonic day 9.5 (E9.5), we observed a clear VD gradient of *Gli1* and *Ptch1* with highest expression levels in the ventral neural tube and a progressive decay toward more dorsal positions (Figure 1D). Overall, mean transcript numbers in the neural tube were significantly lower for *Gli1* than for *Ptch1* (~20 mRNA molecules per cell for *Gli1* and ~150 for *Ptch1* at peak levels). *Gli2* and *Gli3*—the two main contributors to Gli activator and repressor function—were both expressed more highly in the dorsal neural tube than at the ventral end, with *Gli3* displaying significantly more graded expression than *Gli2* (Figure 1E). This data, as well as expression patterns of other established hedgehog targets (Figure S1E), are in concordance with earlier studies (Bai et al., 2004; Dessaud et al., 2008; Lei et al., 2004; Sasaki et al., 1997); however, precise spatial quantification of mRNA levels now enables the application of mathematical modeling.

To simplify data representation, we plotted the absolute transcript densities of target genes in the neural tube as a function of VD position (Figure S1D). We found that expression of both *Gli1* and *Ptch1* reached peak levels at around 15% of the VD distance (Figure 1F). The decay toward more dorsal positions reflects the gradient of diffusing Shh, while the reduced expression levels in the ventral-most 15% of the neural tube correspond to the population of nonneural cells comprising the floor plate region, which become refractory to hedgehog signaling at ~E8.5 (Ribes et al., 2010).

A Simple Thermodynamic Model for Gene Regulation by Bifunctional Transcription Factors

Next, we aimed to develop a simple thermodynamic model (Bintu et al., 2005; Sherman and Cohen, 2012; Zinzen et al., 2006) for gene regulation by bifunctional transcription factors. Such a model should link *Gli1* and *Ptch1* transcript concentrations to activator and repressor levels using only a small number of parameters that can be experimentally determined. We considered a simplified scenario in which a single Gli binding site controls target genes. Activator and repressor forms of Gli1–3 all bind the same binding sites with similar dissociation constants (Hallikas et al., 2006; Müller and Basler, 2000; Peterson et al., 2012), hence, in our model we assume that Gli1–3 activator and repressor can bind competitively with the same dissociation constant K (Figure 2Ai). Importantly, different dissociation constants for activators and repressors would only lead to rescaling of *A* and *R*, and have no influence on model predictions (see below and Supplemental Experimental Procedures). Consequently, three different states of a target gene's Gli binding site can be distinguished: (1) activator-bound, (2) repressor-bound, or (3) free. If we assume equilibrium binding of activator and repressor to the same Gli binding site, the probability for each of these three states is a function of activator and repressor concentrations (*A* and *R*) and the

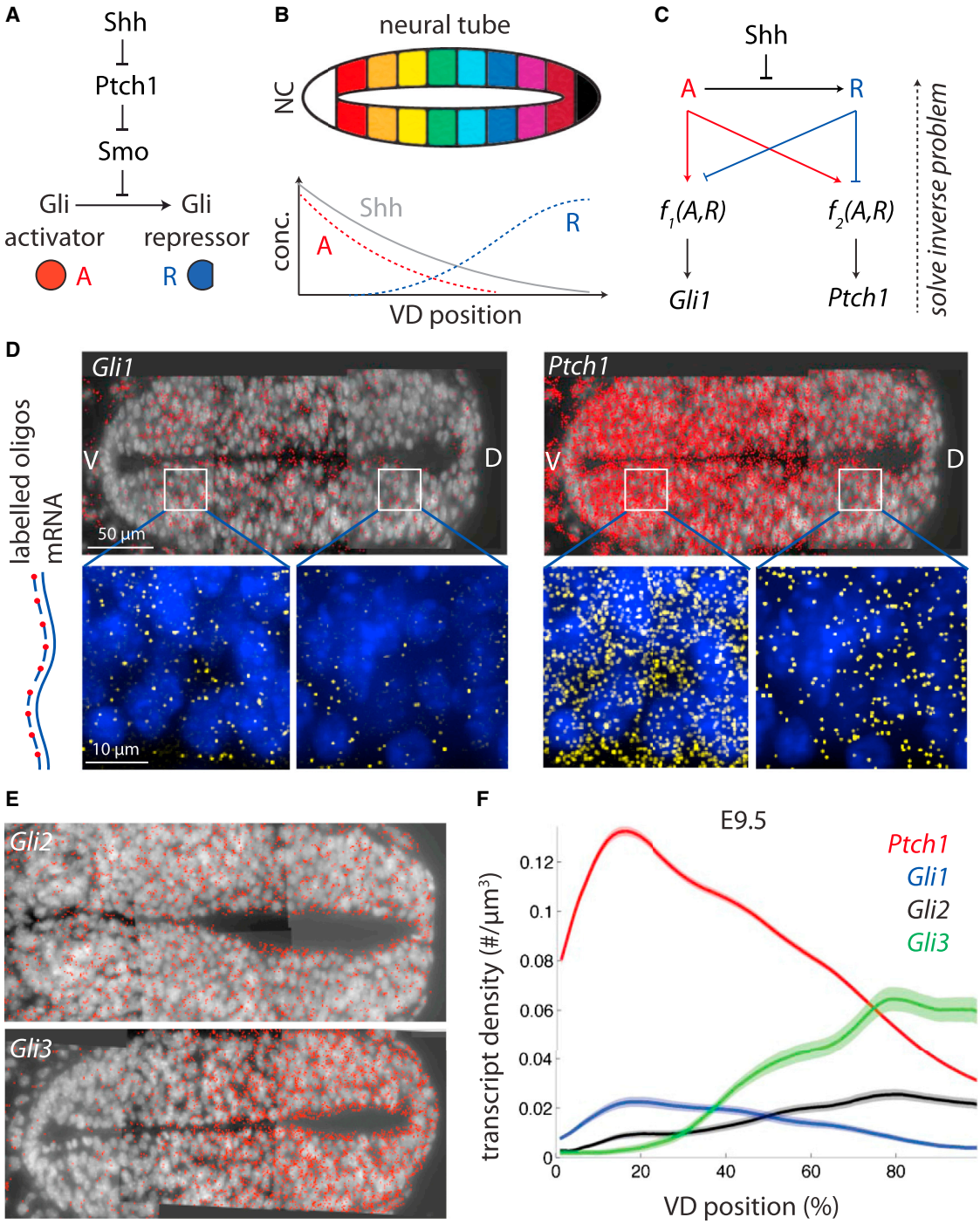

Figure 1. Quantitative Measurements of Gene Expression in Intact Mouse Neural Tube Sections

(A) Shh regulates the balance between activator and repressor forms of Gli factors.

(B) Top: Schematic representation of the neural tube. Bottom: Shh secreted from the notochord (NC) forms a VD gradient (gray line), which is transformed into gradients of activator and repressor forms of Gli (red and blue dashed lines).

(C) The hidden control variables Gli activator and repressor determine gene expression according to the 2D input function of the target gene. Inferring the hidden control variables requires solving the inverse problem.

(D) Stitched image of transverse neural tube section at E9.5 with ventral (V) to dorsal (D) axis extending from left to right. Detected *Gli1* and *Ptch1* mRNA molecules are shown in red. Nuclei are counterstained with DAPI (white). Zoom-ins of maximum z-projection of Laplacian of Gaussian filtered smFISH raw data with DAPI stained nuclei in blue.

(legend continued on next page)

binding site dissociation constant K as described in the following equations,

$$P_A = \frac{\frac{A}{K}}{1+\frac{A}{K}+\frac{R}{K}} \quad P_R = \frac{\frac{R}{K}}{1+\frac{A}{K}+\frac{R}{K}} \quad P_0 = \frac{1}{1+\frac{A}{K}+\frac{R}{K}}, \qquad (1)$$

where P_A, P_R, and P_0 are the probabilities for activator-bound, repressor-bound, and free state, respectively. Since the timescales of Gli protein binding and unbinding are likely to be much faster than any transcriptional feedback loops or changes in Shh levels, equilibrium binding is a valid assumption, even though signaling levels may change over time.

By assigning an output transcript density to each of these three states (α, β, and γ; see Figure 2Aii), we next obtained the following 2D input function for the transcript density m of a hedgehog target gene as a function of A and R (for a more detailed derivation see Supplemental Experimental Procedures):

$$m = \frac{\alpha \cdot \frac{A}{K} + \beta + \gamma \cdot \frac{R}{K}}{1+\frac{A}{K}+\frac{R}{K}}. \qquad (2)$$

As shown in Figure 2Aiii, transcript density reaches maximal value α at high A and low R, and minimal value γ at low A and high R, whereas the basal level β is reached when both A and R are low, as expected. It is important to note that Equation 2 defines a minimal model that contains only regulatory input by Gli transcription factors. Equation 2 is hence not applicable to Gli targets that also integrate other regulatory interactions.

To apply the above mathematical model to activator/repressor control of *Gli1* and *Ptch1*, we needed to determine the parameters for the input functions for these genes. To measure α—the maximal transcript density at very high activator concentrations—we performed directed differentiation of embryonic stem cells into neural progenitors and manipulated hedgehog signaling intensity using the small molecule, Smo agonist (SAG) (Chen et al., 2002). Embryoid bodies (EBs) that are neuralized by retinoic acid (RA) and exposed to SAG, faithfully recapitulate the gene expression pattern of the embryonic neural tube (Peterson et al., 2012; Vokes et al., 2007) and showed maximal transcript densities of α_{Gli1} = 0.09 ± 0.01 μm^{-3} and α_{Ptch1} = 0.27 ± 0.02 μm^{-3} at 24 hr post induction (Figure 2B).

To determine the basal transcription level β, we analyzed *Gli2*$^{-/-}$;*Gli3*$^{-/-}$ compound mutants in which Gli activator and repressor functions are both ablated (Bai et al., 2004; Lei et al., 2004). We measured basal transcript densities of β_{Gli1} = 0.005 ± 0.002 μm^{-3} and β_{Ptch1} = 0.09 ± 0.01 μm^{-3} (Figure 2C). For *Ptch1,* this value applied only to the ventral half of the neural tube, since β_{Ptch1} decreased to 0.06 μm^{-3} in the dorsal-most zone. Basal expression of *Gli1* and *Ptch1* did not change substantially between E8.5 and E9.5, suggesting that basal expression is relatively stable over time.

We found that *Gli1* and *Ptch1* transcription were almost completely absent in the dorsal neural groove at E7.5, while Shh secreted from the notochord had not yet spread through the entire VD axis (Figure 2D). We therefore assumed effective repression at high repressor levels, $\gamma_{Gli1} = \gamma_{Ptch1} = 0$. We found that the overall behavior of the system is relatively insensitive to the value of α and γ, whereas precise measurement of β is important (see below and Figure S3C).

To complete our thermodynamic model, we estimated the ratio of the dissociation constants K_{Ptch1}/K_{Gli1} using three independent methods (the absolute values of the dissociation constants are not important for the further analysis and only act as scaling factors, see Supplemental Experimental Procedures). In a first qualitative approach, we analyzed the Gli binding motifs found within Gli1 binding regions positioned in close proximity to *Gli1* and *Ptch1* (Peterson et al., 2012) (summarized in Table S2). We found that *Gli1* and *Ptch1* both contain high-affinity Gli binding sites, suggesting similar overall dissociation constants. However, a large proportion of the Gli binding sites associated with *Ptch1* match the optimal consensus sequence, whereas the Gli binding sites found near *Gli1* are more divergent. These observations suggest that *Gli1* is regulated by slightly lower affinity binding sites than *Ptch1*.

We next aimed to measure K_{Ptch1}/K_{Gli1} quantitatively. Having determined model parameters α, β, and γ for both genes, and inserting measured wild-type transcript densities m_{Gli1} and m_{Ptch1} in Equation 2, we now have two equations with three unknown variables, A, R, and K_{Ptch1}/K_{Gli1},

$$m_{Gli1} = \frac{\alpha_{Gli1} \cdot \frac{A}{K_{Gli1}} + \beta_{Gli1} + \gamma_{Gli1} \cdot \frac{R}{K_{Gli1}}}{1+\frac{A}{K_{Gli1}}+\frac{R}{K_{Gli1}}}$$
$$m_{Ptch1} = \frac{\alpha_{Ptch1} \cdot \frac{A}{K_{Ptch1}} + \beta_{Ptch1} + \gamma_{Ptch1} \cdot \frac{R}{K_{Ptch1}}}{1+\frac{A}{K_{Ptch1}}+\frac{R}{K_{Ptch1}}}. \qquad (3)$$

In order to solve this underdetermined system, we used two different approaches to achieve R = 0 and simplify Equation 3. First, we compared the transcript density of the two genes at peak signaling levels across all spatial positions and time points (Figure 5A) to the theoretical maximum transcript density as measured in EBs (parameter α_i). Mathematical analysis yielded a value of K_{Ptch1}/K_{Gli1} = 0.55 ± 0.15 for the ratio of the dissociation constants (see Supplemental Experimental Procedures).

Lastly, we used *Gli3*$^{-/-}$ embryos (Figure 4C), where repressor levels are drastically reduced. Substituting R = 0 in Equation 3 and using measured transcript densities in *Gli3*$^{-/-}$ neural tubes, we were able to determine K_{Ptch1}/K_{Gli1} through a linear fit (see Supplemental Experimental Procedures and Figure 2E). We found K_{Ptch1}/K_{Gli1} = 0.60 ± 0.03, confirming the two previous approaches.

(E) Detected *Gli2* and *Gli3* mRNA molecules in neural tube sections at E9.5.
(F) Transcript densities of *Ptch1*, *Gli1*, *Gli2*, and *Gli3* in wild-type neural tube at E9.5 as a function of VD position. Shading corresponds to error bars (95% confidence interval).
See also Figure S1 and Table S1.

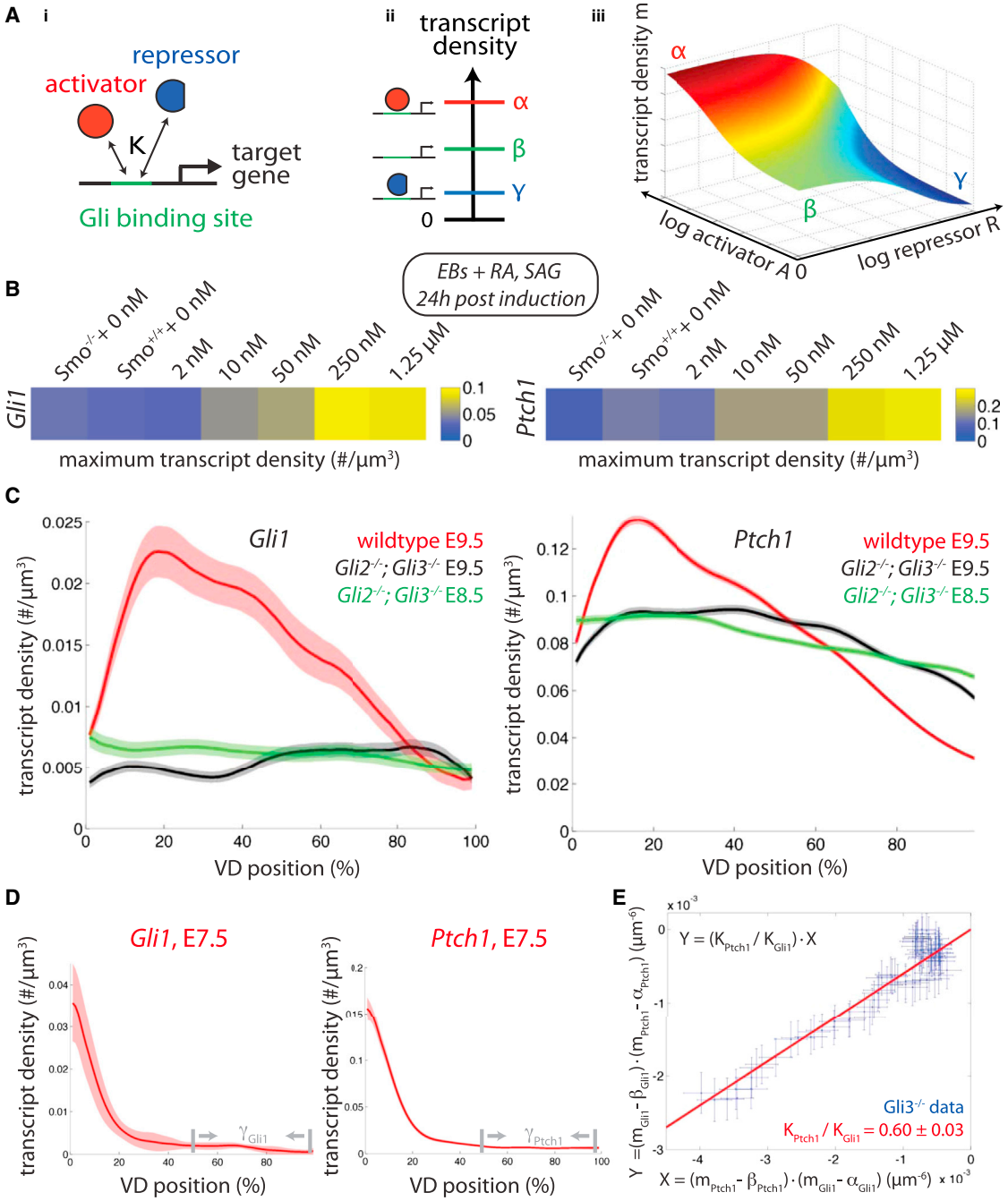

Figure 2. Thermodynamic Model for Gene Regulation through Bifunctional Transcription Factors

(A) Summary of the model, (i) activator and repressor can compete for the same binding site and have identical dissociation constants; (ii) for each target gene, we assign transcript densities α, β, and γ to the three possible occupancy states of the Gli binding site; and (iii) graphical representation of model input function, transcript density as a function of activator and repressor.

(B) Transcript densities of *Gli1* and *Ptch1* in EB sections at different SAG concentrations (24 hr after exposure to RA and SAG).

(C) *Gli1* and *Ptch1* expression in *Gli2*$^{-/-}$; *Gli3*$^{-/-}$ mutant neural tubes at E8.5 and 9.5. Expression in wild-type neural tubes at E9.5 is shown as a reference.

(D) *Gli1* and *Ptch1* transcript density graphs at E7.5, shortly after the onset of *Shh* expression. We measured mean transcript density values in the dorsal half of the neural tube to calculate an upper boundary for γ_{Gli} and γ_{Ptch1}. We found very low values, $\gamma_{Gli1} < 0.0014/\mu m^3$ and $\gamma_{Ptch1} < 0.0063/\mu m^3$. For model calculations, we hence assumed complete repression, $\gamma_{Gli1} = \gamma_{Ptch1} = 0$.

(E) Determination of K_{Ptch1}/K_{Gli1} based on *Gli3*$^{-/-}$ expression data and thermodynamic model for input functions. For details, see Supplemental Experimental Procedures. Error bars were calculated based on Gaussian error propagation of measurement uncertainties.

See also Figure S2 and Table S2.

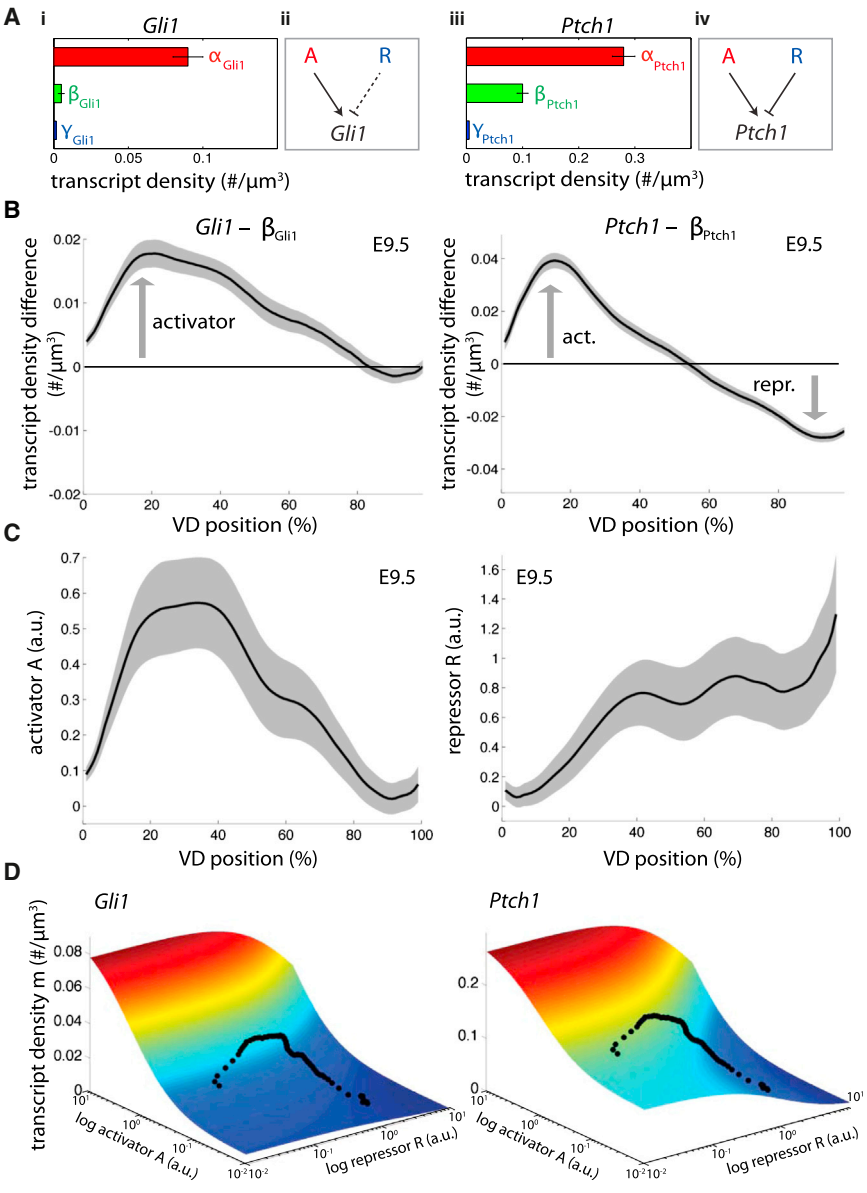

Figure 3. Inferring Hidden Control Variables Based on Transcript Measurements

(A) (i and iii) Experimentally determined parameters α, β, and γ for *Gli1* and *Ptch1*. (ii and iv) Qualitative explanation of different activator/repressor sensitivities. *Gli1* is insensitive to repressor because $\beta \approx \gamma$. For *Ptch1*, $\beta > \gamma$ provides potential for repression.

(B) Difference in gene expression between wild-type and *Gli2*$^{-/-}$;*Gli3*$^{-/-}$ for *Gli1* and *Ptch1*.

(C) Calculated activator and repressor levels in the wild-type neural tube at E9.5 as a function of VD position based upon the model. Shading corresponds to error bars (95% confidence interval), calculated by Gaussian error propagation.

(D) 2D input functions of *Gli1* and *Ptch1*. Wild-type activator and repressor gradients are shown as a trajectory (black) on the transcript density maps. See also Figure S3.

Inferring Hidden Control Variables from Transcript Measurements

The parameters α, β, and γ are summarized in Figures 3Ai and iii. We found that $\beta_{Gli1} \approx \gamma_{Gli1}$, whereas $\beta_{Ptch1} > \gamma_{Ptch1}$. This observation suggested that *Gli1* and *Ptch1* might have different activator and repressor dependencies: in the absence of activator or repressor, *Gli1* and *Ptch1* are expressed at basal levels. Increasing activator levels leads to upregulation of both *Gli1* and *Ptch1* since $\alpha > \beta$; however, if the repressor concentration is increased, only *Ptch1* experiences downregulation ($\beta_{Ptch1} > \gamma_{Ptch1}$), whereas *Gli1* cannot be further reduced ($\beta_{Gli1} \approx \gamma_{Gli1}$). In summary, these data indicate that *Gli1* is relatively insensitive to Gli repressor over a wide concentration range due to its basal transcription levels remaining as low as those in the repressed state (Figures 3Aii and iv).

To illustrate the importance of basal transcription for providing the potential for activation and repression, we plotted wild-type transcript density graphs for *Gli1* and *Ptch1* after subtracting basal transcript densities measured in *Gli2*$^{-/-}$;*Gli3*$^{-/-}$ sections (Figure 3B, left panel). *Gli1* transcription in wild-type animals was always larger than the basal transcript density, suggesting that this gene is in an activator-controlled regime throughout the entire neural tube. In contrast, *Ptch1* expression dropped below basal levels at the dorsal end and was hence subject to repression in this zone, while being dominated by the activator in the ventral neural tube (Figure 3B, right panel).

We next applied our reductionist model to calculate spatial profiles of activator and repressor levels along the neural tube. After having measured all model parameters, we were now able to solve Equation 3 for *A* and *R* in the wild-type neural tube. The inferred activator and repressor gradients along the VD axis are shown in Figure 3C. Note that calculation of *A* and *R* was purely analytical and did not involve any fitting procedure. To account for the remaining gradient of *Ptch1* in *Gli2*$^{-/-}$;*Gli3*$^{-/-}$ neural tubes, we used the position-dependent values of β_{Ptch1} and β_{Gli1} shown in Figure 2C. Importantly, we found smooth opposing gradients for *A* and *R* that decay to zero, even though we did not specify boundary conditions or restrict solutions to positive values.

In Figure 3D, we illustrate the mathematical solutions graphically. *Gli1* and *Ptch1* both have characteristic 2D input functions, based on the parameters discussed above. Next, we plotted the activator and repressor gradients determined in Figure 3C as a trajectory on the input function maps. The activator/repressor trajectory shown in black in Figure 3D is the same for both genes, but the transcript densities along this trajectory are gene-dependent. If we read out the transcript density of *Gli1* and *Ptch1* along the trajectory, we obtain the

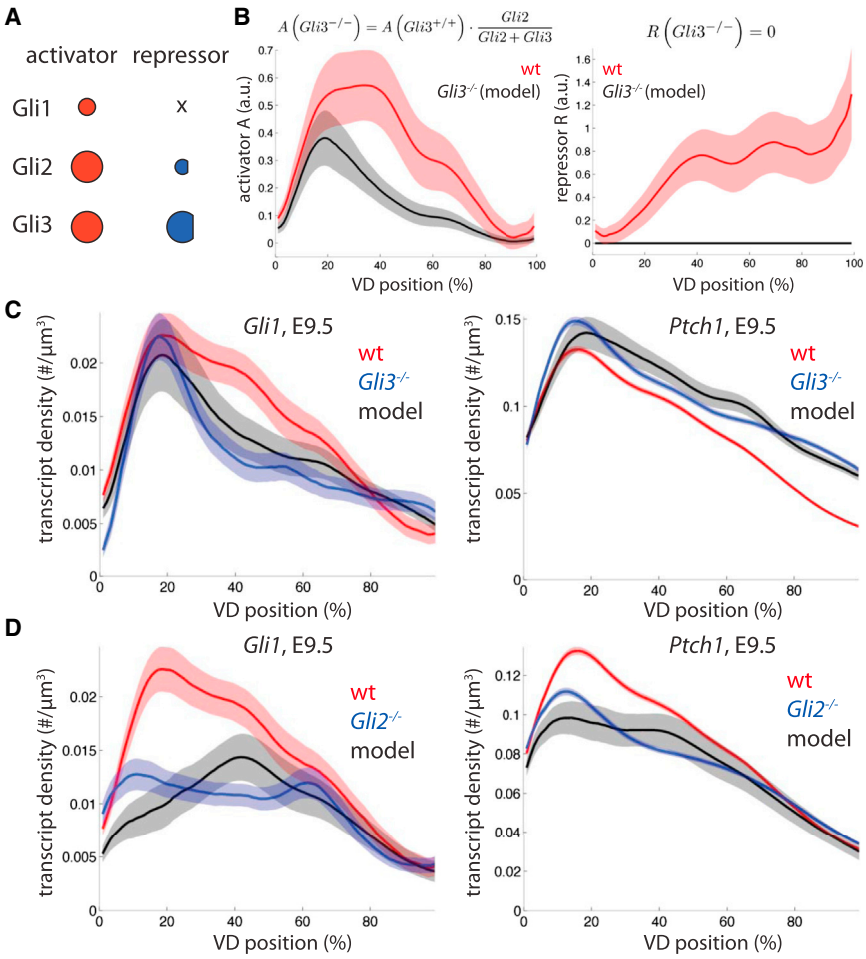

Figure 4. Model Correctly Predicts Gene Expression in Hedgehog Pathway Mutants with Altered Gli Activator and Repressor Levels

(A) Schematic view of relative Gli potencies (see text).

(B) Estimated activator and repressor gradients in *Gli3*$^{-/-}$ neural tube at E9.5 (black). Calculation is based on measurement of *Gli2* and *Gli3* expression and on assumptions discussed in the main text. For comparison, activator and repressor levels in wild-type are shown in red.

(C and D) Predicted transcript densities of *Gli1* and *Ptch1* at E9.5 in *Gli3*$^{-/-}$ (C) and *Gli2*$^{-/-}$ mutants (D) (black). Experimental data are shown in red (wild-type) and blue (mutant).

See also Figure S4 and Data S1.

Predicting Gene Expression in Mutants with Altered Activator and Repressor Levels

As a next step, we aimed to validate our approach by predicting gene expression changes in mutants with altered activator/repressor balance. For this purpose, we estimated the changes in activator and repressor levels in *Gli2*$^{-/-}$ and *Gli3*$^{-/-}$ mutants. Our assumptions for Gli potencies are shown in Figure 4A. We assumed equal potencies of Gli2 and Gli3 in the activator form. Gli2 is believed to have only weak repressor function, since it is mostly degraded in the absence of Shh rather than being processed to a repressor (Pan et al., 2006). Gli1 is a constitutive activator; however, its potency seems to be low, since no phenotype has been observed for *Gli1* knockouts (Bai et al., 2002). In a simplified model, we neglected Gli2 repressor and Gli1 activator function. Hence, repressor levels drop to R = 0 in the *Gli3* mutant (shown in black in Figure 4B, right). Activator levels upon removal of *Gli3* depend on the relative levels of *Gli2* and *Gli3*, and hence on the VD position. Using mRNA levels as a proxy for protein, we obtain,

$$A\left(Gli3^{-/-}\right) = A\left(Gli3^{+/+}\right) \cdot \frac{Gli2}{Gli2+Gli3}. \quad (4)$$

This calculation was performed independently for each position along the VD axis. *Gli2* levels in *Gli3*$^{-/-}$ were undistinguishable from wild-type, suggesting there is no compensation at the level of *Gli* expression in the *Gli3* mutant (data not shown). Using the transcript density measurements for *Gli2* and *Gli3* shown in Figure 1F, we obtained the reduced activator gradient depicted in black in Figure 4B (left).

Solving Equation 3 with these calculated activator and repressor gradients yields predicted transcript densities of *Gli1* and *Ptch1* in the *Gli3*$^{-/-}$ neural tube, shown in black in Figure 4C (experimental data for wild-type is shown in red for comparison). We found that our model predicted downregulation of *Gli1* and upregulation of *Ptch1* in the Gli3$^{-/-}$ neural tube. transcript densities shown in Figure 1F. Hence, while the input function maps show the space of all possible solutions, the activator/repressor trajectory corresponds to the activator/repressor combinations that are actually observed in the neural tube.

The model described above assumes a single Gli binding site for *Gli1* and *Ptch1*, implicitly neglecting cooperative binding of Gli proteins to neighboring Gli binding sites. Since Gli binding cooperativity has been suggested to play a major role in hedgehog-induced pattern formation in *Drosophila* (Parker et al., 2011), we mathematically explored the influence of cooperative binding on our model. For this purpose, we considered a model with two Gli binding sites (Figure S3A and Supplemental Experimental Procedures). Introducing cooperative or anticooperative binding of activators and repressors changed the scaling behavior of activator and repressor gradients without affecting the overall shape of the traces (Figure S3B). The model was also generally robust toward variation of other model parameters (Figure S3C and Supplemental Experimental Procedures). Notably, introducing different dissociation constants for activators and repressors only lead to a trivial rescaling of *A* and *R*. However, the model was relatively sensitive to changes of K_{Ptch1}/K_{Gli1}. Specifically, we obtained negative repressor values when assuming $K_{Gli1} < K_{Ptch1}$.

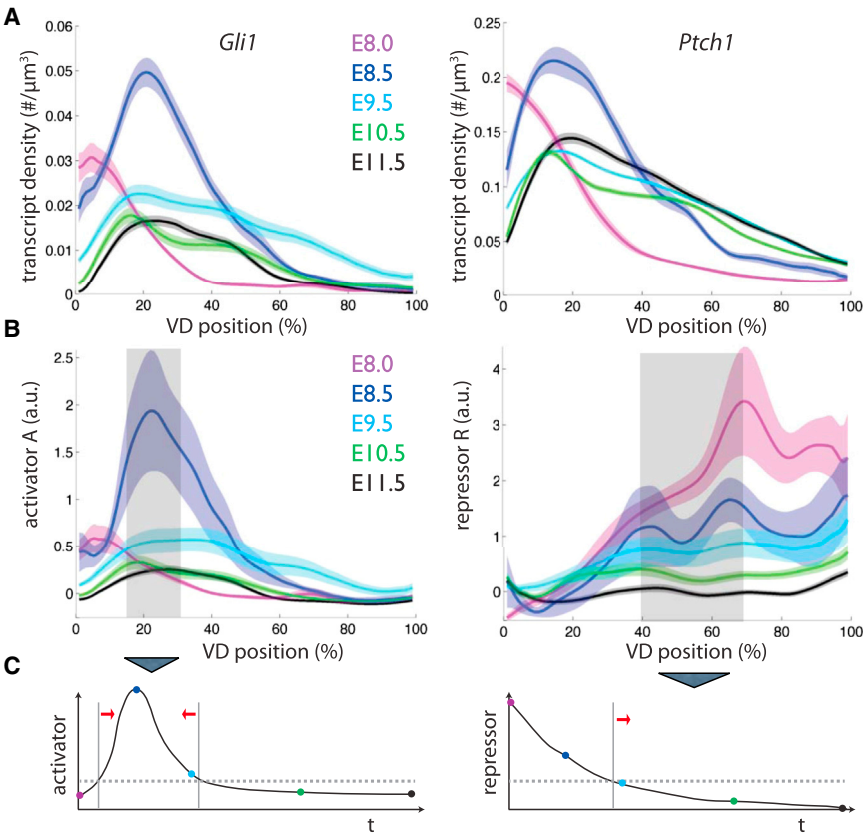

Figure 5. Temporal Analysis of Hedgehog Signaling Reveals Different Dynamics of Activator and Repressor Levels

(A) *Gli1* and *Ptch1* transcription in the neural tube at different developmental time points. Data for *Gli2* and *Gli3* are shown in Figure S5.

(B) Calculated activator and repressor dynamics between E8.0 and E11.5.

(C) Activator and repressor levels as a function of time at the most relevant spatial locations (ventral neural tube for activator and intermediate neural tube for repressor). Time windows allowing expression of target genes are indicated schematically by red arrows, based on an arbitrary threshold (dashed line).

See also Figure S5.

Comparing the prediction to experimental data for the *Gli3* mutant (blue traces), we discovered that the model predicted these opposite effects, as well as the location and magnitude of gene expression changes correctly. We can understand the seemingly contradictory expression changes of *Gli1* and *Ptch1* in $Gli3^{-/-}$ by considering the activator and repressor dependency of these two genes shown in Figures 3Aii and iv. Both activator and repressor are reduced in the *Gli3* mutant, but activator levels are reduced only moderately, while the repressor is completely ablated. For *Ptch1*, which depends on both *A* and *R*, the stronger change of repressor levels is dominant, leading to derepression, and hence, upregulation of transcription. *Gli1*, on the other hand, is much less sensitive to *R* (as long as values of *A* are low), so that its expression change is dominated by the reduction of *A*, leading to reduced activation, and hence, lower transcript levels.

Using the same approach for the *Gli2* mutant, we obtained a reduced activator gradient, while repressor levels remain the same. Again, our model agrees well with experimental data (Figure 4D). However, the deviation between model and experimental data seemed to be slightly larger in $Gli2^{-/-}$ than in $Gli3^{-/-}$ mutant embryos. This effect might be due to the altered gene expression patterns of other direct and indirect hedgehog targets in the *Gli2* mutant, which could potentially feed back on the hedgehog signal. For the *Gli3* mutant at E9.5, on the other hand, we did not find such changes in gene expression of other hedgehog targets (Figure S1F).

We continued to explore the sensitivity of our model to parameter variations by using predicted readout gene expression in $Gli3^{-/-}$ neural tubes as criterion for model performance (Figure S4). Including cooperativity led only to minor changes in predicted gene expression (Figure S4A). Similarly, varying α, β, and γ in a range of possible experimental errors yielded only negligible effects (Figure S4B). Exact values for K_{Ptch1}/K_{Gli1}, however, proved to be crucial for quantitatively correct predictions (Figure S4Bi). Importantly, our simplifying assumption for Gli1–3 potencies (Figure 4A) was not critical for correct model predictions (Figure S4C). Specifically, including Gli1 activator and Gli2 repressor function (50% potency compared to Gli3) led only to very minor differences.

Our model's ability to predict expression changes of pathway readout genes in mutants suggests that the inferred activator and repressor gradients shown in Figures 3C and 3D are representative of the actual activator and repressor levels in embryonic tissue. Hence, we now have a means to determine activator and repressor levels independently at high spatial resolution without the need for genetic manipulation. The smFISH data set, Matlab scripts for inferring *A* and *R*, and scripts for predicting expression traces in mutants are provided as Data S1. We next used this approach as a tool for studying the dynamics of activator and repressor levels in the neural tube.

Temporal Analysis of Hedgehog Signaling Reveals Different Dynamics of Activator and Repressor Levels

Hedgehog signaling in the neural tube is highly dynamic. After reaching peak levels at early developmental stages, overall signaling intensity continually decreases after E8.5 (Balaskas et al., 2012; Peterson et al., 2012). Furthermore, temporal integration of the hedgehog signal has been shown to be important for pattern formation in the neural tube (Dessaud et al., 2007; Stamataki et al., 2005). We therefore decided to examine the temporal dynamics of activator versus repressor levels during neural tube development based on transcript density measurements at different stages of embryonic development (Figures 5A and S5). In agreement with previous work (Balaskas et al., 2012; Peterson et al., 2012), we found maximal transcript levels for *Gli1* and *Ptch1* at E8.5, followed by a decrease at E9.5 and E10.5.

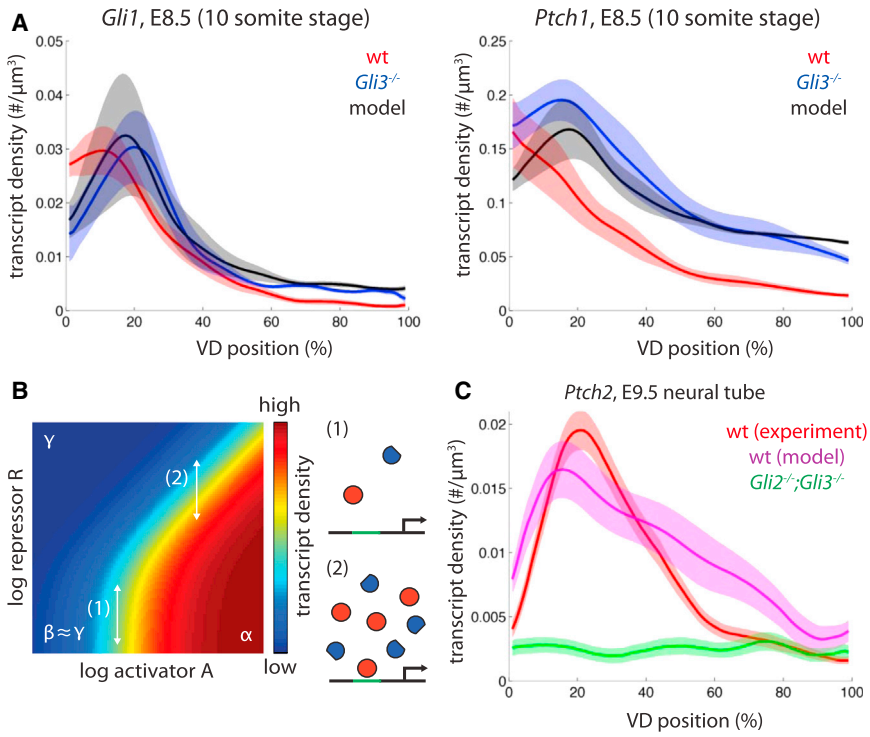

Figure 6. Exploring the Generality of the Model

(A) Predicted transcript densities of *Gli1* and *Ptch1* at E8.5 (somite stage-matched littermates) in the *Gli3* mutant (black). Experimental data are shown in red (wild-type) and blue ($Gli3^{-/-}$). The thermodynamic model predicts expression of *Gli1* and *Ptch1* correctly.

(B) Schematic transcript density map for $\beta \approx \gamma$. White arrows illustrate the effect of changing *R* at different Gli levels. (1) At low Gli concentrations, the target gene is insensitive toward varying repressor concentrations. (2) At high *A* and *R*, the target gene becomes sensitive to *R*, since competition between *A* and *R* is stronger at high Gli concentrations.

(C) *Ptch2* expression traces in the neural tube at E9.5. Wild-type data are shown in red, and basal transcription in $Gli2^{-/-};Gli3^{-/-}$ embryos is shown in green. The predicted wild-type transcript density graph (magenta) is in good agreement with the experimental data.

See also Figure S6.

Using our thermodynamic model, we calculated activator and repressor concentrations for these different time points (Figure 5B). We found that activator levels reached a maximum at E8.5, followed by a rapid decline. The dynamics of the repressor, however, did not show the pulsing behavior observed for the activator. Instead, in our experimental time window, we observed a continuous downregulation of the repressor. The different dynamics of activator and repressor levels are illustrated schematically in Figure 5C, where mean levels at the spatial positions most relevant for pattern formation—the ventral neural tube for the activator and the intermediate neural tube for the repressor (shaded areas in Figure 5B)—are plotted as a function of time. Expression of Gli target genes can be initiated in two ways, either by increasing activator or by reducing repressor concentrations. Using an arbitrary threshold for the initiation of gene expression (dashed line in Figure 5C), we see that the time windows during which expression of target genes is possible are very different for activator and repressor (red arrows in Figure 5C). While activator levels are above the threshold of activation only in a short time window around E8.5, the repressor falls below the threshold of derepression at a later time, and remains below the threshold until the end of our experimental time window.

Exploring the Generality of the Model

The drastic reduction of Gli activator and repressor levels over time allowed us to test the validity of our model in a different parameter range. For this purpose, we compared predicted expression of *Gli1* and *Ptch1* in $Gli3^{-/-}$ neural tubes at E8.5 to experimental data. Using β_{Gli1} and β_{Ptch1} as determined at E8.5 (Figure 2C), and *Gli2* and *Gli3* transcript densities measured at E8.5 (Figure S5), our model predicted gene expression in the $Gli3^{-/-}$ neural tube at E8.5 correctly (Figure 6A). Interestingly, unlike at E9.5, we did not detect a reduction of *Gli1* in $Gli3^{-/-}$ embryos at E8.5, but rather a slight increase. We can understand this effect by considering the schematic transcript density map shown in Figure 6B. As discussed above, genes with low basal transcription ($\beta \approx \gamma$) can be insensitive to repressor concentration. This is, however, only true at low concentrations of *A* and *R*. At high concentrations, even genes with $\beta \approx \gamma$ become sensitive to *R* because competition between activator and repressor for the binding sites becomes substantial (white arrows in Figure 6B). The fact that we experimentally confirmed this prediction provides a further important validation of our model.

To explore the generality of the model further, we aimed to apply our approach to different genes. Many hedgehog targets are also subject to additional regulatory interactions, such as other signaling pathways and tissue-specific competence factors. Perhaps most importantly, many of the well-established hedgehog targets in the neural tube are transcription factors that are involved in cross-repressive interactions (Dessaud et al., 2008). To avoid confounding effects, it is thus important to carefully select genes whose regulation is dominated by Gli activator and repressor levels. *Ptch2* (Motoyama et al., 1998), a non-tissue-specific coreceptor of the pathway, fulfills these criteria and was hence selected for further model validation. We first determined model parameters for *Ptch2* analogously to our approach for *Gli1* and *Ptch1*. We found that *Ptch2* has the lowest parameter value for α and the highest Gli binding site affinity K among the three genes we investigated (Figure S6). Similar to *Gli1*, basal expression β is very low for *Ptch2* (green trace in Figure 6C). With these parameters, and *A* and *R* as determined in Figure 3C, we predicted *Ptch2* expression in the wild-type neural tube without any additional fit parameters, using Equation 2 as the input function. The model reproduced the graded expression pattern of *Ptch2* and peak expression levels very well (Figure 6C). However, it is important to note

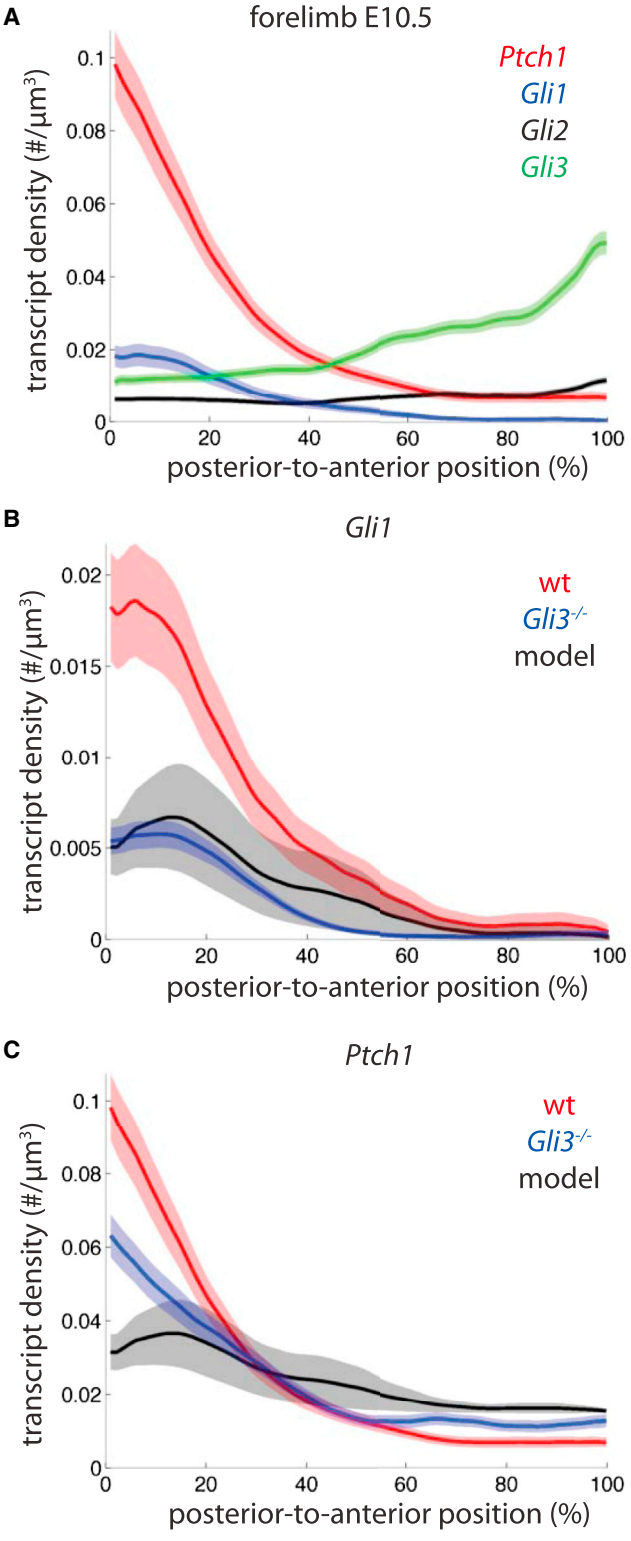

Figure 7. Applying the Model to the Mouse Embryonic Forelimb

(A) Transcript densities of *Ptch1*, *Gli1*, *Gli2*, and *Gli3* along the posterior-to-anterior axis in wild-type forelimbs at E10.5.

(B and C) *Gli1* and *Ptch1* transcript densities in wild-type (red) and *Gli3*$^{-/-}$ (blue) forelimbs at E10.5. Model predictions are shown in black.

See also Figure S7.

that Figure 6C shows a real prediction without any free model parameters. It is hence not surprising that we observe minor expression differences. In particular, we experimentally observed a somewhat steeper gradient for *Ptch2* than predicted by the model, suggesting that the input function for *Ptch2* might be steeper than for *Gli1* and *Ptch1*. The model furthermore correctly predicted that *Ptch2* expression should remain practically unchanged in the *Gli3*$^{-/-}$ neural tube (data not shown).

We next aimed to validate whether our approach can also be successfully applied to different tissues and organs. As a second model system we chose the embryonic forelimb, where Shh is expressed from the zone of polarizing activity, establishing a posterior-to-anterior gradient of Shh (Bénazet and Zeller, 2009). We measured transcript density graphs of *Ptch1*, *Gli1*, *Gli2*, and *Gli3* in wild-type forelimbs at E10.5 (Figure 7A). Since basal transcript density β can contain regulatory contributions by other pathways, we reasoned that this parameter is most likely to vary in different tissues. We hence determined the parameter β in forelimbs, obtaining $\beta_{Gli1} \approx 0.0005/\mu m^3$ and $\beta_{Ptch1} \approx 0.018/\mu m^3$ (data not shown). Based on wild-type *Gli1* and *Ptch1* gradients, we then calculated *A* and *R* along the posterior-to-anterior axis of the wild-type forelimb at E10.5 (red traces in Figure S7). We next estimated *A* and *R* in *Gli3*$^{-/-}$ forelimbs (black traces in Figure S7) and predicted *Gli1* and *Ptch1* expression in the forelimbs of *Gli3*$^{-/-}$ mutants (Figures 7B and 7C). We found that the model was in good agreement with experimental data. This proof-of-principle experiment suggests that the same model can correctly describe the activator and repressor dependence of hedgehog readouts in different tissues.

DISCUSSION

A General Approach for Inferring Hidden Control Variables for Gene Expression

The interplay of different upstream regulators for controlling gene expression is often unclear, particularly in cases where regulators cannot be directly measured with sufficient precision in intact tissues. Here, we mathematically infer hidden control variables of hedgehog signaling—Gli activator and repressor—by measuring transcriptional outputs of signaling in intact tissue sections (Figures 1D–1F) and by developing a minimal model for the input functions of hedgehog target genes (Figure 2A). For this approach it is important to select genes that are faithful reporters of hedgehog signaling and that do not depend on other regulatory contributions. A schematic summary of our approach is shown in Figure 1C. In our model, we assume equilibrium binding of activator and repressor molecules to the same binding site, and we assign different output transcript densities to each occupancy state. Importantly, all model parameters were measured experimentally, using a combination of in vivo and in vitro approaches (Figures 2B–2E). For our analysis, precise quantification of absolute transcript levels using smFISH is crucial for disentangling the contributions of the two upstream regulators. Using short-lived mRNA molecules instead of more long-lived protein reporters such as GFP fluorescence allows us to achieve very high temporal resolution. This is a crucial advantage of our approach, given the highly dynamic nature of hedgehog signaling in the developing neural tube. The approach we present here is broadly

applicable and could be used for studying the integration of multiple signaling factors controlling target genes in many other contexts besides hedgehog signaling.

Unified Model for Activator and Repressor Control by Bifunctional Transcription Factors

Our analysis provides a reductionist model for the dualism of activator versus repressor control in hedgehog signaling. Importantly, our method reveals a surprising simplicity in gene regulation by bifunctional Gli transcription factors. Competitive binding of activators and repressors to the same binding sites can explain all observed gene expression changes of hedgehog readouts in mutants at different developmental stages and in different tissues, including nontrivial opposing changes of *Gli1* and *Ptch1* in the *Gli3*$^{-/-}$ neural tube at E9.5. Cooperativity, different affinities for activators and repressors, and binding preferences of Gli1–3, do not seem to be essential to understand expression changes of these genes in the mutant embryos. Basal transcription and binding site affinity, however, emerge as major determinants for activator versus repressor dependence of target genes. There are two conditions that have to be fulfilled for a gene to be dependent solely on activator or repressor input. First, basal transcription β has to be close to α (insensitive to *A*) or γ (insensitive to *R*) (see Figure 3A). Second, overall Gli protein levels (*A*+*R*) have to be low, so that the binding site is in the unbound state β for a significant fraction of time (see Figure 6B). Both conditions are fulfilled for *Gli1* at E9.5 (see Figure 4C; downregulation of *Gli1* in *Gli3*$^{-/-}$ neural tube). At E8.5, however, the second condition begins to break down, leading to increased repressor dependence of *Gli1* (see Figure 6A; slight increase of *Gli1* in *Gli3*$^{-/-}$ neural tube). Thus, cells sense the ratio *A*/*R* at high Gli concentrations, but can become insensitive to either *A* or *R* at low Gli concentrations.

Gli1 and *Ptch1* are ideal candidate genes for disentangling the regulatory contributions of *A* and *R*, since their expression seems to be dominated by hedgehog signaling. Other Gli targets may integrate input from different signaling pathways, may require tissue-specific competence factors, or may be part of complex gene regulatory networks. Hence, their Gli activator/repressor dependence might be overpowered by other, dominant regulatory inputs that are currently not included in the input functions. In this perspective, our study constitutes only one facet of pattern formation in the neural tube. In a similarly reductionist approach, Balaskas et al. (2012) have demonstrated the importance of mutually repressive interactions between hedgehog targets for pattern formation in the neural tube. Other recent studies have highlighted the importance of *Sox* genes as competence factors for neural-specific expression of hedgehog targets (Oosterveen et al., 2013; Peterson et al., 2012). The ultimate goal of these different lines of research should be to create a combined mathematical model that has the power to predict spatiotemporal gene expression patterns on the genome-wide level and in different wild-type and mutant tissues.

Differences in binding cooperativity between Gli activator and repressor have been proposed as a mechanism for hedgehog-induced pattern formation in *Drosophila* (Parker et al., 2011). Interestingly, differential cooperativity is not required to explain expression changes of *Gli1* and *Ptch1* in mutant mouse embryos, despite the existence of multiple Gli binding sites for both genes. We speculate that repressor cooperativity models might be suboptimal for distinguishing activator-regulated genes from repressor-regulated genes in the mouse, since vertebrate Gli binding motifs seem to exhibit much less sequence divergence than those of *Drosophila* (Parker et al., 2011; Peterson et al., 2012). However, we would like to note that our results do not exclude cooperativity or other regulatory interactions, since our model is relatively insensitive to these factors.

Activator/repressor dualism in the Wnt pathway is established in a way that is very similar to hedgehog signaling: Tcf/Lef transcription factors can act as activators or repressors depending on Wnt ligand levels (Figure S1A). Similar to Gli proteins, different Tcf/Lef factors seem to exhibit different potencies in the activator and repressor state (Cadigan and Waterman, 2012; Merrill et al., 2004). The work presented here can serve as a conceptual framework for studying activator versus repressor control in Wnt signaling, as well as in other cell-cell signaling pathways. Similar to our approach for hedgehog signaling, transcriptional targets involved in feedback regulation might also be good candidates when studying other pathways, since loci encoding feedback regulators are often the simplest readouts of signaling pathways.

Biological Implications of Activator/Repressor Dualism in Hedgehog Signaling

Using our model to measure activator and repressor gradients independently, we find that the levels of Gli activator and repressor follow very different dynamics (Figures 5B and 5C). Interestingly, the process of temporal adaptation and desensitization seems to lead to a zero-hedgehog state that is characterized by the absence of activator and repressor, rather than a repressed state, and is hence different from the initial conditions at the onset of *Shh* expression. We can thus tentatively define three stages of hedgehog-induced pattern formation in the neural tube, "repressed" (before the onset of Shh expression, ~E7.5), "instructive" (high *A*, low *R*, ~E8.0–E9.0), and "permissive" ($A \approx R \approx 0$, ~E9.5–E11.5). Indeed, expression of hedgehog targets in the neural tube is initiated around E8.5, at peak activator levels in the instructive state (Jeong and McMahon, 2005). The permissive zero-hedgehog state might provide a good framework for defining precise boundaries due to cross-repressive interactions between genes expressed in adjacent stripes (Balaskas et al., 2012).

The embryonic forelimb is another interesting model system for hedgehog signaling. While many design principles, such as temporal integration of the hedgehog signal, are analogous to the neural tube, the severity of the *Gli2*$^{-/-}$ phenotype is much stronger in the neural tube than in the forelimb, and vice versa for *Gli3*$^{-/-}$ (Ahn and Joyner, 2004). Our approach yields activator and repressor gradients that are similar to the neural tube, suggesting that the hedgehog pathway operates in comparable ways in the two tissues. Comparing expression of *Ptch1*, *Gli1*, *Gli2*, and *Gli3* in the neural tube and the forelimb, we find similar patterns of graded expression (Figures 1F and 7A). A notable difference, however, is that the ratio *Gli3*/*Gli2* in the forelimb is higher than in the neural tube, in particular in the region closest to the signaling center (ventral neural tube and posterior forelimb). As a consequence, gene expression changes in *Gli3*$^{-/-}$ embryos in this zone are stronger for the forelimb than for the neural tube: expression of *Gli1* and *Ptch1* decreases substantially in the posterior forelimb of *Gli3*$^{-/-}$ mutants at E10.5, while

remaining almost constant in the ventral neural tube at E9.5 (Figures 4C, 7B, and 7C). This observation demonstrates the importance of quantitative and spatially resolved measurements of mRNA levels for the interpretation of genetic experiments. Experimental data for the *Gli3*$^{-/-}$ forelimb is in good agreement with model predictions (Figures 7B and 7C), suggesting that the same unified model can describe hedgehog signaling in different tissues. Hence, we believe that the model presented here can help clarify differences between different tissues with respect to e.g., the relative importance of Gli activator versus repressor for pattern formation. Exploring tissue-specific effects, including additional regulatory interactions, and extending the analysis to other signaling systems that are regulated by bifunctional transcription factors will be important tasks for future research. We anticipate that the combination of spatially resolved quantitative gene expression measurements, genetic manipulation, and mathematical modeling will emerge as a powerful tool to gain fascinating insights into the design principles of signaling systems during development and beyond.

EXPERIMENTAL PROCEDURES

Generation of Mutant Mice

Mouse colonies for *Smo* (Zhang et al., 2001), *Gli2* (Mo et al., 1997), and *Gli3* (Maynard et al., 2002) were maintained as previously described. Compound mutants were generated from timed matings of double heterozygous mice and genotyped by PCR using extraembryonic yolk sac tissue. All studies involving vertebrate animals were performed with institutional approval in compliance with institutional guidelines.

Embryos were collected and fixed for 1 hr in 4% paraformaldehyde and cryoprotected overnight in 30% sucrose/4% paraformaldehyde prior to embedding in tissue freezing medium. For neural tube analysis, we used eight micrometer cryosections taken at the level of the forelimb (heart level before E9.5) for hybridizations. For embryos younger than E9.5, the number of somites was used for precise staging. For forelimb analysis, longitudinal sections perpendicular to the left-right axis were taken at the level of the central forelimb. Experiments were performed independently with multiple tissue sections from at least three different embryos and gave reproducible results.

Generation of Gli2ΔN Embryonic Stem Cells

An N-terminally truncated, active form of mouse *Gli2* carrying an in-frame N-terminal 3×FLAG tag (Sigma) was cloned into the pBigT shuttle vector, then into pRosa26PA (Srinivas et al., 2001). The linearized construct was electroporated into YFP3-1 (Rosa26YFP/β-gal) embryonic stem (ES) cells (Mao et al., 2005) and neomycin-resistant colonies that passed initial visual screens (loss of β-gal or YFP expression) were assayed by southern blot. One resulting ES cell line, Gli2ΔN, was used for further experiments.

Embryoid Bodies

V6.5 embryonic stem cells (ESC) were cultured under standard conditions (15% fetal bovine serum + leukemia inhibitory factor). Neuralized EBs were formed as previously described (Wichterle et al., 2002). Briefly, ESCs were seeded in low attachment 6-well plates (Corning) at a density of 5×10^5 ESC per well and cultured in DFNK (Dulbecco's Modified Eagle Medium:F12, neurobasal media + 10% knockout serum replacement). After 48 hr, EBs were treated with different concentrations of SAG (Cal Biochem) and RA (0.5 μM). Fixation, cryoprotection, and sectioning were performed analogously to mouse embryos.

smFISH and Image Analysis

Fluorescent probes for smFISH were constructed as previously described (Raj et al., 2008). In short, we designed libraries consisting of up to 96 oligonucleotides of 20 nucleotides length, complementary to the coding sequences of the genes of interest (see Table S1 for probe sequences). Probes were coupled to different fluorophores (Cy5, Alexa594, and TMR) to allow detection of up to three genes in the same tissue sections. Hybridizations were performed overnight at 30°C as previously described (Itzkovitz et al., 2012; Raj et al., 2008). DAPI dye for nuclear staining was added during the washes after hybridization. Images were taken with a Nikon Ti-E inverted fluorescence microscope equipped with a 100× oil-immersion objective and a Photometrics Pixis 1024B CCD camera using MetaMorph software (Molecular Devices). We recorded stacks of images (z spacing 0.3 μm) at adjacent x-y positions covering the entire VD axis of neural tube sections.

Diffraction-limited dots corresponding to single mRNA molecules were automatically detected using custom Matlab software, based on previously described algorithms (Raj et al., 2008). Briefly, the images were first filtered using a 3D Laplacian of Gaussian filter with a width of 15 pixels and a SD of 1.5 pixels (Figure S1B). We then determined the intensity threshold at which the number of connected components was least sensitive to the threshold (Itzkovitz et al., 2012) (Figure S1C). Individual images were stitched in Matlab using stage coordinates and cross-correlation analysis.

Data Analysis and Mathematical Modeling

Transcript density graphs were calculated in a stripe along the VD axis with lateral width of 20 μm, using a sliding window with a length of 10% of the VD axis for smoothing (Figure S1D). Colored patches in transcript density graphs show 95% confidence intervals around the mean. Error bars for inferred variables and model predictions were calculated based on Gaussian error propagation of measurement uncertainties for *Ptch1*, *Gli1*, *Gli2*, and *Gli3* transcript densities. Mathematical modeling was performed in Matlab, as described in the Supplemental Experimental Procedures.

SUPPLEMENTAL INFORMATION

Supplemental Information includes Supplemental Experimental Procedures, seven figures, two tables, and one data file and can be found with this article online at http://dx.doi.org/10.1016/j.devcel.2014.10.017.

AUTHOR CONTRIBUTIONS

J.P.J. and A.v.O. conceived and designed the project, with input from K.A.P. and A.P.M. J.P.J. performed smFISH experiments, analyzed the data, and developed the thermodynamic model. K.A.P. and Y.N. prepared mouse embryo samples. K.A.P. prepared embryoid body samples. J.M. generated *Gli2ΔN* ESC. J.P.J. wrote the manuscript with input from A.v.O., K.A.P., and A.P.M. All authors discussed and interpreted results.

ACKNOWLEDGMENTS

We thank Shalev Itzkovitz and Nicola Crosetto for helpful discussions and comments on the manuscript. J.P.J. was supported by a Feodor Lynen fellowship (Alexander von Humboldt Foundation). This work was supported by a European Research Council (ERC) Advanced grant (ERC-AdG 294325-GeneNoiseControl), a Nederlandse Organisatie voor Wetenschappelijk Onderzoek (NWO) Vici award, and the NIH/National Cancer Institute Physical Sciences Oncology Center at Massachusetts Institute of Technology (U54CA143874). Work in A.P.M.'s laboratory was supported by a grant from the NIH (NS033642).

Received: June 27, 2014
Revised: September 5, 2014
Accepted: October 24, 2014
Published: November 24, 2014

REFERENCES

Ahn, S., and Joyner, A.L. (2004). Dynamic changes in the response of cells to positive hedgehog signaling during mouse limb patterning. Cell *118*, 505–516.

Bai, C.B., Auerbach, W., Lee, J.S., Stephen, D., and Joyner, A.L. (2002). Gli2, but not Gli1, is required for initial Shh signaling and ectopic activation of the Shh pathway. Development *129*, 4753–4761.

Bai, C.B., Stephen, D., and Joyner, A.L. (2004). All mouse ventral spinal cord patterning by hedgehog is Gli dependent and involves an activator function of Gli3. Dev. Cell *6*, 103–115.

Balaskas, N., Ribeiro, A., Panovska, J., Dessaud, E., Sasai, N., Page, K.M., Briscoe, J., and Ribes, V. (2012). Gene regulatory logic for reading the Sonic Hedgehog signaling gradient in the vertebrate neural tube. Cell *148*, 273–284.

Barolo, S., and Posakony, J.W. (2002). Three habits of highly effective signaling pathways: principles of transcriptional control by developmental cell signaling. Genes Dev. *16*, 1167–1181.

Bénazet, J.-D., and Zeller, R. (2009). Vertebrate limb development: moving from classical morphogen gradients to an integrated 4-dimensional patterning system. Cold Spring Harb. Perspect. Biol. *1*, a001339.

Bintu, L., Buchler, N.E., Garcia, H.G., Gerland, U., Hwa, T., Kondev, J., and Phillips, R. (2005). Transcriptional regulation by the numbers: models. Curr. Opin. Genet. Dev. *15*, 116–124.

Buecker, C., and Wysocka, J. (2012). Enhancers as information integration hubs in development: lessons from genomics. Trends Genet. *28*, 276–284.

Cadigan, K.M., and Waterman, M.L. (2012). TCF/LEFs and Wnt signaling in the nucleus. Cold Spring Harb. Perspect. Biol. *4*, a007906–a007906.

Chen, J.K., Taipale, J., Young, K.E., Maiti, T., and Beachy, P.A. (2002). Small molecule modulation of Smoothened activity. Proc. Natl. Acad. Sci. USA *99*, 14071–14076.

Dessaud, E., Yang, L.L., Hill, K., Cox, B., Ulloa, F., Ribeiro, A., Mynett, A., Novitch, B.G., and Briscoe, J. (2007). Interpretation of the sonic hedgehog morphogen gradient by a temporal adaptation mechanism. Nature *450*, 717–720.

Dessaud, E., McMahon, A.P., and Briscoe, J. (2008). Pattern formation in the vertebrate neural tube: a sonic hedgehog morphogen-regulated transcriptional network. Development *135*, 2489–2503.

Hallikas, O., Palin, K., Sinjushina, N., Rautiainen, R., Partanen, J., Ukkonen, E., and Taipale, J. (2006). Genome-wide prediction of mammalian enhancers based on analysis of transcription-factor binding affinity. Cell *124*, 47–59.

Haskel-Ittah, M., Ben-Zvi, D., Branski-Arieli, M., Schejter, E.D., Shilo, B.-Z., and Barkai, N. (2012). Self-organized shuttling: generating sharp dorsoventral polarity in the early Drosophila embryo. Cell *150*, 1016–1028.

Hui, C.-C., and Angers, S. (2011). Gli proteins in development and disease. Annu. Rev. Cell Dev. Biol. *27*, 513–537.

Itzkovitz, S., Lyubimova, A., Blat, I.C., Maynard, M., van Es, J., Lees, J., Jacks, T., Clevers, H., and van Oudenaarden, A. (2012). Single-molecule transcript counting of stem-cell markers in the mouse intestine. Nat. Cell Biol. *14*, 106–114.

Jeong, J., and McMahon, A.P. (2005). Growth and pattern of the mammalian neural tube are governed by partially overlapping feedback activities of the hedgehog antagonists patched 1 and Hhip1. Development *132*, 143–154.

Kaplan, S., Bren, A., Zaslaver, A., Dekel, E., and Alon, U. (2008). Diverse two-dimensional input functions control bacterial sugar genes. Mol. Cell *29*, 786–792.

Kim, H.D., and O'Shea, E.K. (2008). A quantitative model of transcription factor-activated gene expression. Nat. Struct. Mol. Biol. *15*, 1192–1198.

Lei, Q., Zelman, A.K., Kuang, E., Li, S., and Matise, M.P. (2004). Transduction of graded Hedgehog signaling by a combination of Gli2 and Gli3 activator functions in the developing spinal cord. Development *131*, 3593–3604.

Levine, M. (2010). Transcriptional enhancers in animal development and evolution. Curr. Biol. *20*, R754–R763.

Mao, J., Barrow, J., McMahon, J., Vaughan, J., and McMahon, A.P. (2005). An ES cell system for rapid, spatial and temporal analysis of gene function in vitro and in vivo. Nucleic Acids Res. *33*, e155.

Maynard, T.M., Jain, M.D., Balmer, C.W., and LaMantia, A.-S. (2002). High-resolution mapping of the Gli3 mutation extra-toes reveals a 51.5-kb deletion. Mamm. Genome *13*, 58–61.

Merrill, B.J., Pasolli, H.A., Polak, L., Rendl, M., García-García, M.J., Anderson, K.V., and Fuchs, E. (2004). Tcf3: a transcriptional regulator of axis induction in the early embryo. Development *131*, 263–274.

Mo, R., Freer, A.M., Zinyk, D.L., Crackower, M.A., Michaud, J., Heng, H.H., Chik, K.W., Shi, X.M., Tsui, L.C., Cheng, S.H., et al. (1997). Specific and redundant functions of Gli2 and Gli3 zinc finger genes in skeletal patterning and development. Development *124*, 113–123.

Motoyama, J., Heng, H., Crackower, M.A., Takabatake, T., Takeshima, K., Tsui, L.-C., and Hui, C. (1998). Overlapping and non-overlapping Ptch2 expression with Shh during mouse embryogenesis. Mech. Dev. *78*, 81–84.

Müller, B., and Basler, K. (2000). The repressor and activator forms of Cubitus interruptus control Hedgehog target genes through common generic gli-binding sites. Development *127*, 2999–3007.

Oosterveen, T., Kurdija, S., Alekseenko, Z., Uhde, C.W., Bergsland, M., Sandberg, M., Andersson, E., Dias, J.M., Muhr, J., and Ericson, J. (2012). Mechanistic differences in the transcriptional interpretation of local and long-range Shh morphogen signaling. Dev. Cell *23*, 1006–1019.

Oosterveen, T., Kurdija, S., Enstero, M., Uhde, C.W., Bergsland, M., Sandberg, M., Sandberg, R., Muhr, J., and Ericson, J. (2013). SoxB1-driven transcriptional network underlies neural-specific interpretation of morphogen signals. Proc. Natl. Acad. Sci. USA *110*, 7330–7335.

Pan, Y., Bai, C.B., Joyner, A.L., and Wang, B. (2006). Sonic hedgehog signaling regulates Gli2 transcriptional activity by suppressing its processing and degradation. Mol. Cell. Biol. *26*, 3365–3377.

Parker, D.S., White, M.A., Ramos, A.I., Cohen, B.A., and Barolo, S. (2011). Thecis-regulatory logic of Hedgehog gradient responses: key roles for gli binding affinity, competition, and cooperativity. Sci. Signal. *4*, ra38.

Peterson, K.A., Nishi, Y., Ma, W., Vedenko, A., Shokri, L., Zhang, X., McFarlane, M., Baizabal, J.M., Junker, J.P., van Oudenaarden, A., et al. (2012). Neural-specific Sox2 input and differential Gli-binding affinity provide context and positional information in Shh-directed neural patterning. Genes Dev. *26*, 2802–2816.

Raj, A., van den Bogaard, P., Rifkin, S.A., van Oudenaarden, A., and Tyagi, S. (2008). Imaging individual mRNA molecules using multiple singly labeled probes. Nat. Methods *5*, 877–879.

Ribes, V., Balaskas, N., Sasai, N., Cruz, C., Dessaud, E., Cayuso, J., Tozer, S., Yang, L.L., Novitch, B., Martí, E., and Briscoe, J. (2010). Distinct Sonic Hedgehog signaling dynamics specify floor plate and ventral neuronal progenitors in the vertebrate neural tube. Genes Dev. *24*, 1186–1200.

Sasaki, H., Hui, C., Nakafuku, M., and Kondoh, H. (1997). A binding site for Gli proteins is essential for HNF-3beta floor plate enhancer activity in transgenics and can respond to Shh in vitro. Development *124*, 1313–1322.

Segal, E., Raveh-Sadka, T., Schroeder, M., Unnerstall, U., and Gaul, U. (2008). Predicting expression patterns from regulatory sequence in Drosophila segmentation. Nature *451*, 535–540.

Setty, Y., Mayo, A.E., Surette, M.G., and Alon, U. (2003). Detailed map of acis-regulatory input function. Proc. Natl. Acad. Sci. USA *100*, 7702–7707.

Sherman, M.S., and Cohen, B.A. (2012). Thermodynamic state ensemble models ofcis-regulation. PLoS Comput. Biol. *8*, e1002407.

Srinivas, S., Watanabe, T., Lin, C.S., William, C.M., Tanabe, Y., Jessell, T.M., and Costantini, F. (2001). Cre reporter strains produced by targeted insertion of EYFP and ECFP into the ROSA26 locus. BMC Dev. Biol. *1*, 4.

Stamataki, D., Ulloa, F., Tsoni, S.V., Mynett, A., and Briscoe, J. (2005). A gradient of Gli activity mediates graded Sonic Hedgehog signaling in the neural tube. Genes Dev. *19*, 626–641.

Vokes, S.A., Ji, H., McCuine, S., Tenzen, T., Giles, S., Zhong, S., Longabaugh, W.J.R., Davidson, E.H., Wong, W.H., and McMahon, A.P. (2007). Genomic characterization of Gli-activator targets in sonic hedgehog-mediated neural patterning. Development *134*, 1977–1989.

Wichterle, H., Lieberam, I., Porter, J.A., and Jessell, T.M. (2002). Directed differentiation of embryonic stem cells into motor neurons. Cell *110*, 385–397.

Zhang, X.M., Ramalho-Santos, M., and McMahon, A.P. (2001). Smoothened mutants reveal redundant roles for Shh and Ihh signaling including regulation of L/R symmetry by the mouse node. Cell *106*, 781–792.

Zinzen, R.P., Senger, K., Levine, M., and Papatsenko, D. (2006). Computational models for neurogenic gene expression in the Drosophila embryo. Curr. Biol. *16*, 1358–1365.

Zinzen, R.P., Girardot, C., Gagneur, J., Braun, M., and Furlong, E.E.M. (2009). Combinatorial binding predicts spatio-temporalcis-regulatory activity. Nature *462*, 65–70.